INORGANIC CHEMISTRY
FRONTIERS

RESEARCH ARTICLE

View Article Online
View Journal | View Issue

Cite this: *Inorg. Chem. Front.*, 2018, **5**, 1409

An enhanced power factor *via* multilayer growth of Ag-doped skutterudite $CoSb_3$ thin films

Zhuang-Hao Zheng,[a,b] Meng Wei,[a] Jing-Ting Luo,[a] Fu Li,[a] Guang-Xing Liang,[a] Yan Liang,[a] Jin Hao,[a] Hong-Li Ma,[b] Xiang-Hua Zhang[b] and Ping Fan *[a]

Received 8th March 2018,
Accepted 26th March 2018

DOI: 10.1039/c8qi00207j

rsc.li/frontiers-inorganic

Skutterudite $CoSb_3$ has emerged as one of the most studied candidate materials for thermoelectric applications. In this work, the multilayer inter-diffusion method for depositing Ag-doped $CoSb_3$ thin films was used to improve its thermoelectric property. A microstructure study demonstrates that Ag enters into the lattice. By using first-principles calculations, it can be concluded that the Ag atoms will preferentially occupy the lattice voids, rather than substitute Sb or Co rings, leading to better thermoelectric performance. As expected, the increase of both Seebeck coefficient and electric conductivity is obtained after Ag doping through the multilayer diffusion method, indicating that this approach can resolve the conflict between these often-contractive thermoelectric factors. Due to this efficient combined action, the power factor has substantially been enhanced and the maximum value reaches 0.11 mW m^{-1} K^{-2} at 573 K, which is five times higher than that of the un-doped sample.

1. Introduction

Thermoelectric (TE) materials have the ability to directly convert thermal energy to electricity and *vice versa*.[1] Thus, TE materials have gained great interest due to their potential applications in many fields, including direct conversion of waste heat from industrial sectors or automobile exhausts to electricity, and solid state Peltier coolers.[2] The performance of TE materials is related to the dimensionless thermoelectric figure of merit, ZT, determined by the Seebeck coefficient (S), electrical conductivity (σ), and thermal conductivity (κ) as $ZT = S^2\sigma/\kappa$, where $S^2\sigma$ is also defined as the power factor (PF) and κ includes electronic thermal conductivity κ_{ele} and lattice thermal conductivity κ_{lat} ($\kappa = \kappa_{ele} + \kappa_{lat}$).[3] Since S, σ and κ_{ele} are interrelated and generally conflicting *via* carrier concentration, it is a longstanding challenge to largely improve the TE performance. Therefore, concepts or strategies that can decouple these parameters to simultaneously optimize the electron and phonon transport are highly encouraged and imperative for the thermoelectric community.[4–6] $CoSb_3$ has drawn extensive attention as one of the most promising TE materials in the intermediate temperature range over the past few decades.[7–10] It crystallizes in a body-centered cubic structure with space group $Im3$ and a unit cell consists of 32 atoms, in which Co atoms form eight sub-cubes with pnicogen rings occupying six of them, leaving the final two voids or cages empty. This special lattice vacancy of the skutterudite structure can be filled within ions that increases the Seebeck coefficient and reduces thermal conductivity by increasing the charge carrier mass and with the "rattling" effect due to the additional phonon scattering centres.[11,12] For instance, G. Rogl *et al.*[13] demonstrated that In-doped multi-filled n-type skutterudites can exhibit a high power factor and very low thermal conductivity, leading to an outstanding ZT value of 1.8 at 823 K.

Recently, the increasing demand of microscale energy harvesting for mobile electronic devices has stimulated the investigation of multifunctional thin film TE devices, which have many advantages such as flexibility, light weight, small volume, high integration, and enhanced compatibility.[14–19] Additionally, thin films, as one type of low-dimension materials, have good TE performance due to their dense interfaces and grain boundaries, which can effectively scatter phonons.[20] Therefore, many studies on the synthesis of high performance thin films, including $CoSb_3$ films, have been investigated.[21–26] For example, A. Ahmed *et al.*[27] obtained a power factor of 7.92 mW m K^{-2} for the $CoSb_2$-containing mixed phase thin film and 1.26 mW m K^{-2} for the stoichiometric $CoSb_3$ thin film. However, TE properties of $CoSb_3$ thin films remain lower than those of bulk materials due to the difficulty of controlling precisely the composition of the thin films.

Radio frequency (RF) magnetron sputtering is an attractive technique to prepare high quality thin films for industrial development.[28] We have successfully fabricated $CoSb_3$ thin films with a pure skutterudite structure by using this tech-

[a]*Institute of Thin Film Physics and Applications, Shenzhen Key Laboratory of Advanced Thin Films and Applications, College of Physics and Energy, Shenzhen University, 518060, China. E-mail: fanping308@126.com*
[b]*Laboratory of Glasses and Ceramics, Institute of Chemical Science UMR CNRS 6226, University of Rennes 1, Rennes 35042, France*

nique in our previous studies.[29–31] However, the TE performance of the films is still inadequate and needs further improvement. In this work, Ag was used as a dopant and the multilayer growing method has been employed which has been reported[32–34] as an efficient way to prepare doped $CoSb_3$ films with a large choice of elements. The influence of the Ag doping content on the micro-structure and thermoelectric properties will be investigated.

2. Experimental details

The Ag target (99.99%) and Co–Sb (99.95%) alloy target with a Co/Sb atomic ratio of 1 : 3.5 were fixed in a magnetron sputtering facility, equipped with a three-position rotatable target system. The sputtering angle was 45° and the target-substrate distance was 10 cm. 2 cm × 2 cm × 1.5 mm glass substrates were used and cleaned in an ultrasonic bath for 10 minutes in acetone, 10 min in absolute ethyl alcohol and 10 min in deionized water. The vacuum chamber was firstly pumped down to 8.0×10^{-4} Pa and the working pressure was kept at 0.4 Pa with an argon flow of 40 sccm. At first, a Co–Sb layer was deposited onto the glass substrate with a sputtering power of 50 W and the deposition time was 7.5 min. A Ag layer was then deposited onto the previous Co–Sb layer by using a sputtering power of 1 W. For this layer, the deposition time was adjusted for controlling the Ag content. Then, a 2nd Co–Sb layer was deposited again with the same experimental conditions as the primary Co–Sb layer. Lastly, an annealing process was used for all the samples at 325 °C for 1 hour under a constant flow of argon. The precise composition as a function of Ag deposition time was analyzed by energy dispersive spectroscopy and summarized in Table 1.

The crystalline phases were determined by X-ray diffraction (XRD) (*D*/max2500, Rigaku Corporation) with the 2θ angle range of 15°–70°, using Cu K_α radiation (λ = 0.15406 nm). The lattice parameters were refined using the full-profile Rietveld refinement method. Room temperature Raman scattering measurements were performed by using a spectra system Lab Ram Xplora (Horiba Jobin Yvon). The laser excitation used in this work was the 514.5 nm line of an Ar^+ ion laser. X-ray photoelectron spectroscopy (Escalab 250Xi) was used to investigate the chemical states of the thin film. The micro-structure was characterized by using scanning electron microscopy (SEM, Zeiss supra 55) and transmission electron microscopy (TEM, JEM-3200FS) while the composition analysis was performed by energy dispersive spectroscopy (EDS). The electrical conductivity and Seebeck coefficient were simultaneously measured in the interval of 298 K–573 K by using a Nezsch-SBA458 equipment. The carrier concentration was measured by Van der Pauw Hall measurement (HL5500PC, Nanometrics) at room temperature.

In order to determine whether the Ag dopant is energetically favorable, first principles calculations are carried out with the context of density functional theory (DFT) with plane-wave basis sets, as implemented in the Vienna *ab initio* Simulation Package (VASP).[35–37] All the calculations were performed with the PBE exchange–correlation functional, and the projected augmented wave (PAW) approach with a plane wave cutoff of 400 eV. The calculations of all the doped systems were done with a 5 × 5 × 5 *k* grid. The convergence criteria are set to be 10^{-4} eV in energy and 0.02 eV $Å^{-1}$ in force.

We estimated the cohesive energy E_{coh} of the Ag-doped $CoSb_3$ supercell according to the following formula:[38]

$$E_{coh} = (E_{Ag\text{-}CoSb_3} - xE_{Ag} - yE_{Sb} - zE_{Co})/(x + y + z) \quad (1)$$

where $E_{Ag\text{-}CoSb_3}$, E_{Ag}, E_{Sb} and E_{Co} are the total energies of the supercell with Ag dopants, single Ag atom, single Sb atom and Co atom, respectively. *x*, *y* and *z* are the number of Ag, Sb and Co atoms, respectively.

3. Results and discussion

Fig. 1(a) shows the XRD patterns of Ag doped $CoSb_3$ thin films, including the un-doped sample. The diffraction peaks of all the samples can be indexed to the body-centered cubic skutterudite phase with space group $Im\bar{3}$ (PDF#78-0976). There are no impurity phases within the detection limit of the XRD spectrometer, indicating that all the films have single $CoSb_3$ phase. As shown in the inset, the peaks slightly shift to a small angle and the shift increases with increasing Ag content, suggesting the crystal cell expansion. The lattice parameters as a function of Ag content have been calculated using the XRD data and the results are shown in Fig. 1(b). It can be found that the lattice parameter increases obviously after Ag doping, suggesting that the Ag element entered into the lattice. Although the lattice parameter increases with increasing Ag content, it tends to a stable value when the Ag content is over 1.9%. This non-linear trend is similar to the behaviour of the filled bulk $CoSb_3$ materials,[39,40] indicating Ag is likely filling into the voids of the lattice.

Raman analysis was performed in the range of 70 cm^{-1} to 220 cm^{-1} shift for all the samples and the results are presented in Fig. 2. Four modes were observed in the patterns of all the samples at the positions of 106 cm^{-1}, 131 cm^{-1}, 146 cm^{-1} and 178 cm^{-1}, corresponding respectively to the F_{g2}, E_{g1}, A_{g1} and A_{g2} Raman sensitive phonon vibration modes in $CoSb_3$ predicted by theoretical simulation.[33] No extra peak can be observed, confirming that the films have single cubic structure which is consistent with the XRD result. It is notable that the vibration modes are unchanged and have almost the same peak intensity and full width at half maximum before and after Ag doping. This phenomenon reveals that the cubic structure has a stable bonding state. However, the peaks shift to a lower value as already observed with the XRD results, con-

Table 1 Ag content of the thin films as a function of Ag deposition time

Ag deposition time (s)	0	2	4	6	8	10
Ag content (at%)	0	0.4	1.5	1.9	2.2	2.7

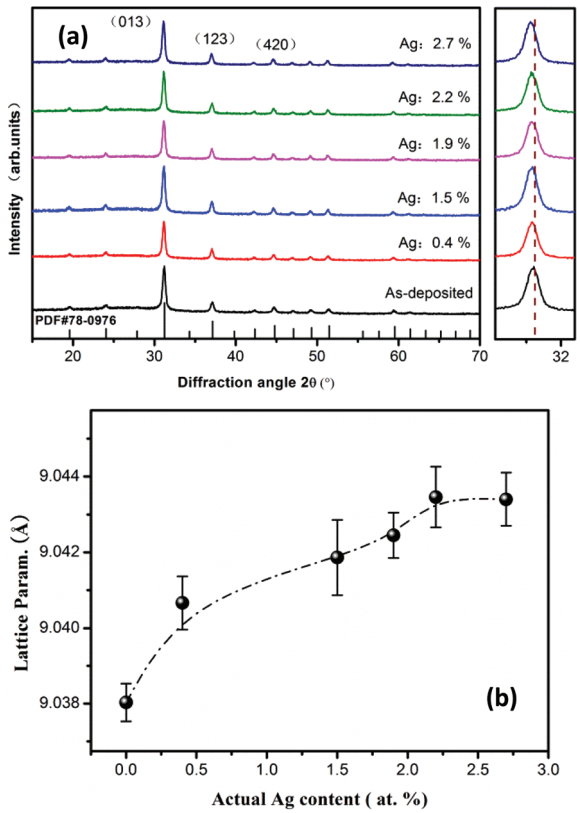

Fig. 1 (a) The XRD patterns of un-doped and Ag doped $CoSb_3$ thin films and (b) the lattice parameters, calculated using the XRD data, as a function of Ag contents.

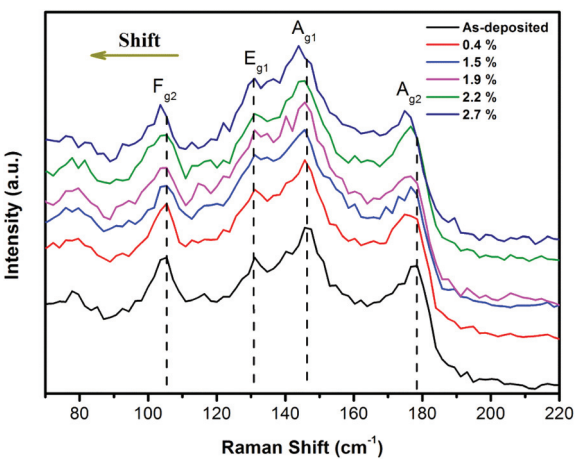

Fig. 2 The results of Raman spectra in the range of 70 cm^{-1} to 220 cm^{-1} shift for all the specimens.

firming the lattice expansion. Therefore, it can be confirmed that this dynamic disorder is produced by the insertion of Ag atoms into the lattice.

To further confirm the Ag state in the lattice, we have performed first-principles DFT calculations. Fig. 3 shows the cohesive energy as a function of concentration for various Ag

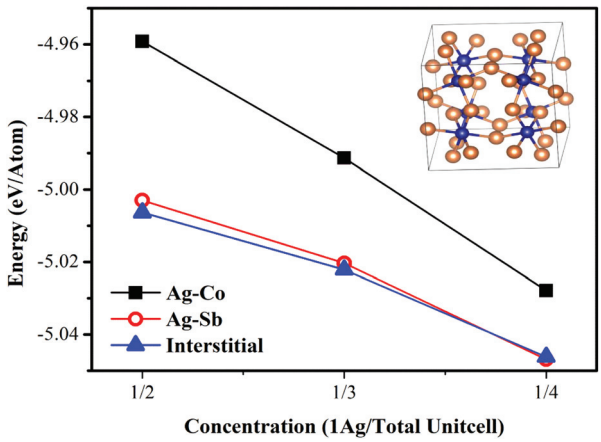

Fig. 3 The cohesive energy as a function of Ag concentration.

locations. As shown in Fig. 3, it is much easier to substitute Sb or to stay at interstitial sites for Ag as the calculated E_{coh} values are much lower than that of substituting Co. With the increase of Ag concentration, the absolute energy value decreases and the absolute E_{coh} values of interstitial Ag become maximum. Additionally, Sb-excess was present in all the samples in this work and it was less likely that Ag (being smaller than Sb) substitutes Sb as the lattice parameters were rising with increasing Ag-content. Thus, it can be concluded that the Ag atoms will preferentially occupy the lattice voids, rather than substituting the Sb or Co rings.

In order to investigate the valence states of the films, XPS analysis was conducted. The binding energy (BE) obtained from the high-resolution core level spectra regions of Co 2p, Sb 3d and Ag 3d of the undoped thin film and the sample with a Ag content of 2.2% is shown in Fig. 4. The BE of all peaks was corrected using C 1s energy at 284.8 eV in addition to the charge compensation by the flood gun associated with the spectrometer. The spin–orbit-coupled doublet of Co 2p core levels of the undoped sample is split into 2p3/2 (779.0 eV) and 2p1/2 (793.7 eV) with the separation of the 2p doublet by 14.7 eV and it is attributed to the charge state of Co^{3+}. The Ag-doped sample has the same BE separation (14.9 eV), indicating that the sample has a stable Co state. However, the chemical shift to a lower value means that the filled Ag reduces the p–d orbital hybridization between Co and Sb. It can be seen from the undoped film that the photoemission spectra of Sb 3d5/2 and 3d3/2 core levels are both composed of double peaks. The two deconvoluted peaks of the photoemission spectra of Sb 3d5/2 and 3d3/2 core levels in $CoSb_3$ are obtained by Gaussian–Lorentzian deconvolution analysis, showing that the Sb in $CoSb_3$ has a metallic and oxidized state. The photoemission spectrum of the Sb 3d core level in the Ag-doped sample is almost the same as that of the undoped $CoSb_3$. According to the bonding states in $CoSb_3$, the chemical states of Sb in $CoSb_3$ include both Co–Sb and Sb–Sb bonds. Thus, combining the results of Co and Sb core level spectra, the Ag doping has no effect on the chemical state of Sb–Sb rings.

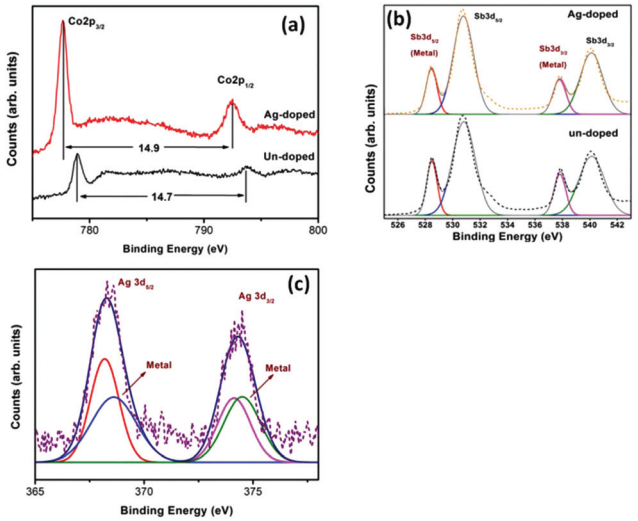

Fig. 4 The binding energy (BE) obtained from the high-resolution core level spectral regions of Co 2p (a), Sb 3d (b) and Ag 3d (c) of the undoped thin film and the sample with a Ag content of 2.2%.

Similar results have been found in previous reports on doped $CoSb_3$ materials with enhanced thermoelectric performance.[41,42] In the case of Ag, the BE of Ag 3d5/2 and Ag 3d3/2 was around 368.3 and 374.5 eV, which is the typical position and separation of spin–orbit components for Ag ion$^+$. It seems that the photoemission spectra of Ag 3d core levels are composed of satellite peaks including probably the metal state.

Fig. 5 displays the surface morphology for all the samples. It can be seen that the undoped sample contains some tiny grains. Similar results can be observed for all the Ag doped

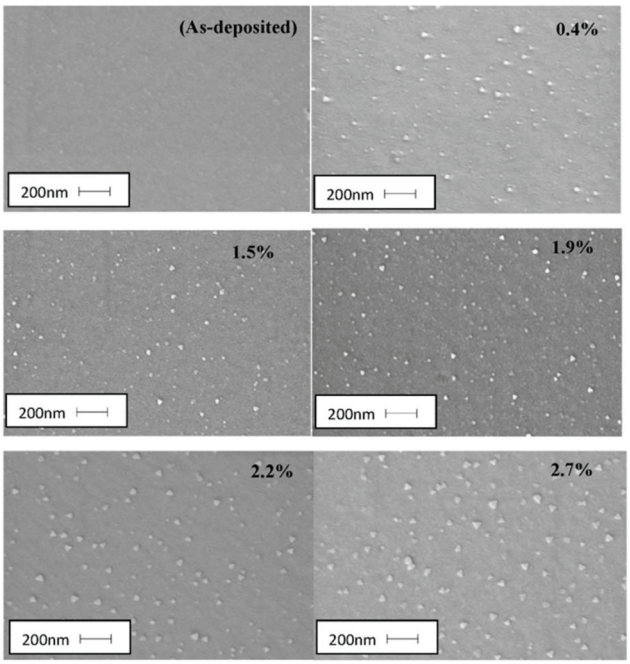

Fig. 5 SEM surface morphology of all the samples.

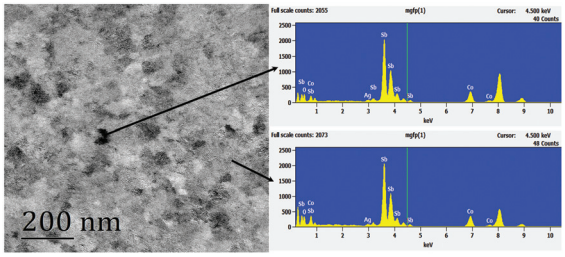

Fig. 6 TEM image of the sample with a Ag content of 2.7%.

samples. With the increase of Ag content, the particles become larger and triangle-shaped, suggesting that Ag can promote the grain growth. Fig. 6 shows the TEM image of the sample with a Ag content of 2.7%. It can be found that there are some black and white regions, which might be due to the protruding particles on the surface. The insert images of composition analysis show few and insignificant differences between these regions. In addition, the elemental mappings shown in Fig. 7 indicate that all the elements were homogenously distributed in the thin films. Thus, we deduce that the observed white grains dispersed on the surface have the same structure and composition as the thin film.

Fig. 8(a), (b) and (c) show respectively the electrical conductivity σ, the Seebeck coefficient S and the power factor PF as a function of temperature. In Fig. 8(b), σ of the undoped sample is 0.83×10^4 S m^{-1} at 298 K which is a relatively low value compared to bulk materials. It distinctly increases with increasing temperature, suggesting semiconductor characteristics. The electrical conductivity σ is obviously increased after Ag-doping with the same trend as the un-doped sample. Comparatively, the sample with a Ag content of 2.2% shows the highest electrical conductivity at 298 K, but the sample doped with 1.5% Ag has a maximum absolute value of 1.82×10^4 S m^{-1} at 523 K. However, the electrical conductivity of all the samples decreases dramatically when the temperature is over 523 K and drops to extremely low values after the temperature is increased above 573 K. This result can be attributed to

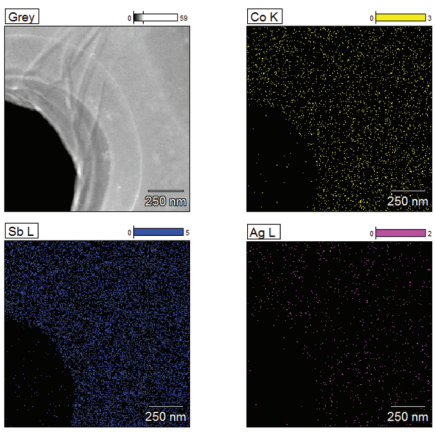

Fig. 7 The elemental mappings.

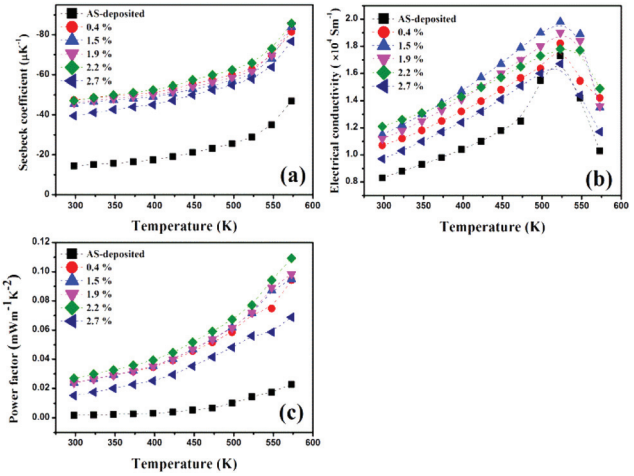

Fig. 8 The temperature dependence of thermoelectric properties (a) electrical conductivity; (b) Seebeck coefficient; (c) power factor.

the intensity of the oxidation defect, resulting in the decline of σ.

The Seebeck coefficients S for the films are shown in Fig. 8(b) and display a negative sign over the entire temperature range, indicating the N-type behaviour. The absolute S value of the un-doped sample is in the range of 15–40 μV K^{-1}. The S value is greatly increased for all Ag doped samples and it reaches a maximum with a Ag doping of 2.2%. As all the Ag-doped films have larger absolute S values than that of the un-doped sample, it can be concluded that Ag is an effective dopant. The maximum absolute S value can be observed to be 86 μV K^{-1} at 573 K, which is two times higher than the value for the undoped sample.

It is worth noting that both Seebeck coefficient S and electrical conductivity σ are increasing at appropriate Ag doping, demonstrating that Ag doping can resolve the conflict between S and σ. It is well known that the electrical conductivity is determined by the expression of $\sigma = n\mu e$, where n is the carrier concentration, μ is the carrier mobility and e is the unit charge. And the Seebeck coefficient is also related to the carrier concentration and the density of states effective mass of carriers, according to the Pisarenko relations:[43]

$$S = \frac{8\pi^2 {k_B}^2}{3eh^2} m^* T \left(\frac{\pi}{3n}\right)^{2/3} \quad (2)$$

where k_B is the Boltzmann constant, e is the electron charge, h is the Planck constant, and m^* is the density of states effective mass of carriers. It can be found that S and σ are both dependent on carrier concentration n. Therefore, the Hall carrier concentration n of all the samples at room temperature was measured. For the undoped samples, the carrier concentration is 1.9×10^{21} cm^{-3} and it increases to 5.8×10^{21} cm^{-3} when the Ag content is 0.4% and the n of all the Ag doped samples is higher than this value. The increase of n is attributed to the additional electron carrier created by Ag doping, resulting in the increase of σ, since the Seebeck coefficient is inversely proportional to the carrier concentration. Thus, we deduce that the increase of the Seebeck coefficient of our doped samples is mainly due to the increased electron effective mass, as already observed with other doped $CoSb_3$ materials, having an effective mass between 2 and $3m_0$ (the free electron mass) after doping.[44–47]

The power factor PF calculated from the measured σ and S is plotted in Fig. 8(c). Due to the increase of both Seebeck coefficient and electrical conductivity originated by Ag doping, the PF has been obviously enhanced and increases with increasing Ag content. The PF value of all Ag-doped samples is much higher than that of the un-doped sample, and the sample with a Ag content of 2.2% shows a maximum value of 0.11 mW m^{-1} K^{-2} at 573 K, which is five times higher than the PF value of the un-doped sample.

4. Conclusions

Ag doped $CoSb_3$ thin films were fabricated by the multilayer growth method and the effect of the Ag content was investigated. Microstructure study and theoretical simulation results confirm that Ag fills into the lattice and occupies the void, with significant effects on the chemical state of Co–Sb bonding. The Seebeck coefficient and the electrical conductivity of the doped thin films are greatly enhanced due to the increasing carrier concentration and density of states effective mass of carriers, leading to substantial enhancement of the power factor. These results demonstrate the effectiveness of our concept for simultaneously improving the Seebeck coefficient and electrical conductivity through careful composition doping.

Conflicts of interest

There are no conflicts to declare.

Acknowledgements

This work is supported by the National Natural Science Foundation of China (No. 11604212), Key platform and research projects, Education and Research of Guangdong Province (2015KQNCX139), Basical Research Program of Shenzhen (JCYJ20160307113206388) and Shenzhen Key Lab Fund (ZDSYS 20170228105421966).

References

1 L. E. Bell, *Science*, 2008, **321**, 1457.
2 F. J. DiSalvo, *Science*, 1999, **285**, 703.
3 G. J. Snyder and E. S. Toberer, *Nat. Mater.*, 2008, **7**, 105.
4 K. Biswas, J. He, I. D. Blum, C. I. Wu, T. P. Hogan, D. N. Seidman, V. P. Dravid and M. G. Kanatzidis, *Nature*, 2012, **489**, 414.

5 Y. Hu, L. P. Zeng, A. J. Minnich, M. S. Dresselhuas and G. Chen, *Nat. Nanotechnol.*, 2015, **10**, 701.
6 B. C. Sales, D. Mandrus and R. K. Williams, *Science*, 1996, **272**, 1325.
7 J. P. Heremans, V. Jovovic, E. S. Toberer, A. Saramat, K. Kurosaki, A. Charoenphakdee, S. Yamanaka and G. J. Snyder, *Science*, 2008, **321**, 554.
8 W. Y. Zhao, P. Wei, Q. J. Zhang, H. Peng, W. T. Zhu, D. G. Tang, J. Yu, H. Y. Zhou, Z. Y. Liu, X. Mu, D. Q. He, J. C. Li, C. L. Wang, X. F. Tang and J. H. Yang, *Nat. Commun.*, 2015, **6**, 6197.
9 T. J. Zhu, Y. T. Liu, C. G. Fu, J. P. Heremans, J. G. Snyder and X. B. Zhao, *Adv. Mater.*, 2017, **29**, 1605884.
10 W. Y. Zhao, Z. Y. Liu, P. Wei, Q. J. Zhang, W. T. Zhu, X. L. Su, X. F. eng Tang, J. H. Yang, Y. Liu, J. Shi, Y. M. Chao, S. Q. Lin and Y. Z. Pei, *Nat. Nanotechnol.*, 2017, **12**, 55.
11 M. Christensen, A. B. Abrahamsen, N. B. Christensen, F. Juranyi, N. H. Andersen, K. Lefmann, J. Andreasson, C. R. H. Bahl and B. B. Iversen, *Nat. Mater.*, 2008, **7**, 811.
12 H. Chi, H. Kim, J. C. Thomas, X. Su, S. Stackhouse, M. Kaviany, A. V. Ven, X. Tang and C. Uher, *Phys. Rev. B: Condens. Matter Mater. Phys.*, 2012, **86**, 195209.
13 G. Rogl, *Acta Mater.*, 2015, **95**, 201.
14 K. I. Uchida, H. Adachi, T. Kikkawa, A. Kirihara, M. Ishida, S. Yorozu, S. Maekawa and E. Saitoh, *Proc. IEEE*, 2016, **104**, 1946.
15 P. Fan, Z. H. Zheng, Y. Z. Li, Q. Y. Lin, J. T. Luo, G. X. Liang, X. M. Cai, D. P. Zhang and F. Ye, *Appl. Phys. Lett.*, 2015, **106**, 073901.
16 P. Fan, Z. H. Zheng, Z. K. Cai, T. B. Chen, P. J. Liu, X. M. Cai, D. P. Zhang, G. X. Liang and J. T. Luo, *Appl. Phys. Lett.*, 2013, **102**, 033904.
17 M. S. Dresselhaus, G. Chen, M. Y. Tang, R. G. Yang, H. Lee, D. Z. Whang, Z. F. Ren, J. P. Fleurial and P. Gogna, *Adv. Mater.*, 2007, **19**, 1043.
18 K. F. Hsu, S. Loo, F. Guo, W. Chen, J. S. Dyck, C. Uher, T. Hogan, E. K. Polychroniadis and M. G. Kanatzidis, *Science*, 2004, **303**, 818.
19 R. Venkatasubramanian, T. Colpitts, B. O'Quinn, S. Liu, N. El-Masry and M. Lamvik, *Appl. Phys. Lett.*, 1999, **75**, 1104.
20 J. L. Feldman and D. J. Singh, *Phys. Rev. B: Condens. Matter Mater. Phys.*, 1996, **53**, 6273.
21 H. Anno, T. Sakakibara, Y. Notohara, H. Tashiro, T. Koyanagi, H. Kaneko and K. Matsubara, Proceedings of the 16th International Conference on Thermoelectrics, Dresden, Germany, August 1997, p. 338.
22 J. C. Caylor, A. M. Stacy, R. Gronsky and T. Sands, *J. Appl. Phys.*, 2001, **89**, 3508.
23 V. Savchuk, A. Boulouz, S. Chakraborty, J. Schumann and H. Vinzelberg, *J. Appl. Phys.*, 2002, **92**, 5319.
24 A. Ahmed and S. Han, *Thin Solid Films*, 2015, **587**, 150.
25 M. V. Daniel, M. Lindorf and M. Albrecht, *J. Appl. Phys.*, 2016, **120**, 125306.
26 A. Ahmed and S. Han, *J. Alloys Compd.*, 2016, **686**, 540.
27 A. Ahmed and S. Han, *Appl. Surf. Sci.*, 2017, **408**, 88.
28 P. Fan, Y. Zhang, Z. H. Zheng, W. F. Fan, J. T. Luo, G. X. Liang and D. P. Zhang, *J. Electron. Mater.*, 2015, **44**, 630.
29 Z. H. Zheng, M. Wei, F. Li, J. T. Luo, H. L. Ma, G. X. Liang, X. H. Zhang and P. Fan, *J. Mater. Sci.: Mater. Electron.*, 2017, **28**, 17221.
30 Z. H. Zheng, F. Li, F. Li, Y. Z. Li, P. Fan, J. T. Luo, G. X. Liang, Bo Fan and A. H. Zhong, *Thin Solid Films*, 2017, **632**, 88.
31 Z. H. Zheng, M. Wei, F. Li, J. T. Luo, H. L. Ma, G. X. Liang, X. H. Zhang and P. Fan, *Coatings*, 2017, **7**, 205.
32 M. Stoica and C. S. Lo, *Phys. Rev. B: Condens. Matter Mater. Phys.*, 2012, **86**, 115211.
33 H. Anno, K. Matsubara, T. Caillat and J. P. Fleuial, *Phys. Rev. B: Condens. Matter Mater. Phys.*, 2000, **62**, 16.
34 P. Nieroda, K. Kutorasinski, J. Tobola and K. T. Wojciechowski, *J. Electron. Mater.*, 2014, **43**, 1681.
35 P. E. Blöchl, *Phys. Rev. B: Condens. Matter Mater. Phys.*, 1994, **50**, 17953.
36 J. P. Perdew, K. Burke and M. Ernzerhof, *Phys. Rev. Lett.*, 1996, **77**, 3865.
37 J. P. Perdew and Y. Wang, *Phys. Rev. B: Condens. Matter Mater. Phys.*, 1992, **45**, 13244.
38 G. Z. Zhang and Q. Sun, *J. Phys. Chem. Lett.*, 2016, **7**, 2664.
39 X. Shi, W. Zhang, L. D. Chen and J. Yang, *Phys. Rev. Lett.*, 2005, **95**, 185503.
40 B. R. Ortiz, C. M. Crawford, R. W. McKinney, P. A. Parillab and E. S. Toberer, *J. Mater. Chem. A*, 2016, **4**, 8444.
41 X. Y. Zhou, G. Y. Wang, L. Zhang, H. Chi, X. L. Su, J. Sakamoto and C. Uher, *J. Mater. Chem.*, 2012, **22**, 2958.
42 C. Chen, L. Zhang, J. H. Li, F. R. Yu, D. L. Yu, Y. J. Tian and B. Xu, *J. Alloys Compd.*, 2017, **699**, 751.
43 Y. L. Tang, Z. M. Gibbs, L. A. Agapito, G. D. Li, H. S. Kim, M. B. Nardelli, S. Curtarolo and G. J. Snyder, *Nat. Mater.*, 2015, **14**, 1223.
44 M. Puyet, B. Lenoir, A. Dauscher, M. Dehmas, C. Stiewe and E. Müller, *J. Appl. Phys.*, 2004, **95**, 4852.
45 D. T. Morelli, G. P. Meisner, B. Chen, S. Hu and C. Uher, *Phys. Rev. B: Condens. Matter Mater. Phys.*, 1997, **56**, 7376.
46 G. S. Nolas, M. Kaeser, R. T. Littleton and T. M. Tritt, *Appl. Phys. Lett.*, 2000, **77**, 1855.
47 L. D. Chen, T. Kawahara, X. F. Tang, T. Goto, T. Hirai, J. S. Dyck, W. Chen and C. Uher, *J. Appl. Phys.*, 2001, **90**, 1864.

